Article

High-Pressure Torsion: A Path to Refractory High-Entropy Alloys from Elemental Powders

Andrey Mazilkin [1], Mahmoud R. G. Ferdowsi [2], Evgeniy Boltynjuk [1], Roman Kulagin [1] and Rimma Lapovok [2,*]

1   Institute of Nanotechnology, Karlsruhe Institute of Technology, 76344 Eggenstein-Leopoldshafen, Germany; andrey.mazilkin@partner.kit.edu (A.M.); evgeniy.boltynjuk@kit.edu (E.B.); roman.kulagin@kit.edu (R.K.)
2   Institute for Frontier Materials, Deakin University, Waurn Ponds, VIC 3216, Australia
*   Correspondence: r.lapovok@deakin.edu.au

Abstract: For the first time, the refractory high-entropy alloys with equiatomic compositions, HfNbTa-TiZr and HfNbTiZr, were synthesized directly from a blend of elemental powders through ten revolutions of high-pressure torsion (HPT) at room temperature. This method has demonstrated its effectiveness and simplicity not only in producing solid bulk materials but also in manufacturing refractory high-entropy alloys (RHEAs). Unlike the melting route, which typically results in predominantly single BCC phase alloys, both systems formed new three-phase alloys. These phases were defined as the Zr-based hcp1 phase, the α-Ti-based hcp2 phase, and the Nb-based bcc phase. The volume fraction of the phases was dependent on the accumulated plastic strain. The thermal stability of the phases was studied by annealing samples at 500 °C for one hour, which resulted in the formation of a mixed structure consisting of the new two hexagonal and cubic phases.

Keywords: refractory high entropy alloys; blended elemental powders; high-pressure torsion

1. Introduction

High-entropy alloys (HEAs) mark a transformative shift in the field of alloy development, offering diverse compositions and phase structures to enhance material properties [1,2]. The traditional manufacturing method of HEAs, which uses arc-melting, faces some difficulties in achieving chemical homogeneity and the desired phase size and distribution [3–5]. The melting approach, particularly for refractory high-entropy alloys (RHEAs), with their large difference in melting point (e.g., from 1660 °C for Ti to 2996 °C for Ta), can lead to chemical segregation and a dendritic microstructure, with elements such as Nb and Ti predominately clustering within dendrites. To avoid these issues, methods such as faster cooling or extended high-temperature heat treatment are employed, though these solutions can significantly increase costs [3].

An alternative approach is the use of mechanical alloying, conducted at a much lower relative temperature (0.3–0.4 T_m) using elemental metal powders, which circumvents the complications associated with casting. This technique is particularly effective for materials with disparate melting points; it facilitates the creation of alloys and phases, which are not achievable through melting. Our previous study has highlighted the advantages of using severe plastic deformation (SPD) methods, e.g., equal channel angular pressing (ECAP) with back-pressure, to compact powders into solid billets with unique properties not attainable in traditionally cast materials [6]. This process benefits from the intense mechanical work accompanied by diffusion processes within the powder particles. It results in a refined microstructure characterized by a combination of high-angle and low-angle grain boundaries, which enhances diffusive mixing even in metals with low diffusivity, such as those present in RHEAs [7].

Our recent study on HfNbTaTiZr and HfNbTiZr systems showed that mechanical alloying and powder consolidation by ECAP processing followed by ten revolutions of high-pressure torsion (HPT) at room temperature resulted in the formation of a two-phase

BCC/HCP alloy [7]. Short-term annealing at 500 °C following deformation does not lead to a change in the phase composition of the alloy, but it changes the ratio of the volume fractions of the BCC and HCP phases.

The novelty of this work lies in the direct application of HPT at room temperature for the production of RHEA from a mixture of loosely blended elemental (BE) powders without its preliminary compaction. The method used to synthesize the alloys in this study differs from the traditional high-temperature sintering of BE powders [8–10] and proposes a new approach for the fabrication of RHEA through the solid-state consolidation of elemental powders to form phases at room temperature.

Although most currently published works on equiatomic RHEAs indicate a tendency towards the formation of a single BCC phase [1–5], our data indicate the formation of a multiple-phase structure as a result of cold, severe plastic deformation. This study not only aims to extend the understanding of phase formation processes in RHEA; it also explores the potential of HPT at room temperature to overcome the problems inherent in the arc melting route for the synthesis of new materials.

2. Materials and Experimental Procedures

2.1. Powder Consolidation by High Pressure Torsion

This study explores the synthesis of two RHEAs, namely HfNbTaTiZr and HfNbTiZr, using BE powders (mesh 325). The blends were prepared with calculated weight fractions to achieve equiatomic compositions for the alloys, designated as M1 ($Hf_{20}Nb_{20}Ta_{20}Ti_{20}Zr_{20}$) and M2 ($Hf_{25}Nb_{25}Ti_{25}Zr_{25}$). Sample storage and mixture preparation were carried out in a Vigor glove box (Marktheidenfeld, Germany) under an argon atmosphere, maintaining oxygen and moisture levels below 0.002 ppm and 0.1 ppm, respectively.

These powder mixtures were taken from the glove box, poured on the bottom anvil of the HPT rig, and immediately subjected to deformation at room temperature with a rotation velocity of 5 rpm and a hydrostatic pressure of 5 GPa. After ten revolutions, the loose powder was consolidated into discs with a diameter of 10 mm (Figure 1a). The samples after deformation were henceforth designated as LP-M1-HPT and LP-M2-HPT. To investigate the thermal stability of the grain structure and phase composition, part of the deformed samples was annealed at 500 °C for one hour in a vacuum furnace. Samples after annealing were cooled down with the furnace; the corresponding samples were further designated as LP-M1-HPT-An and LP-M2-An.
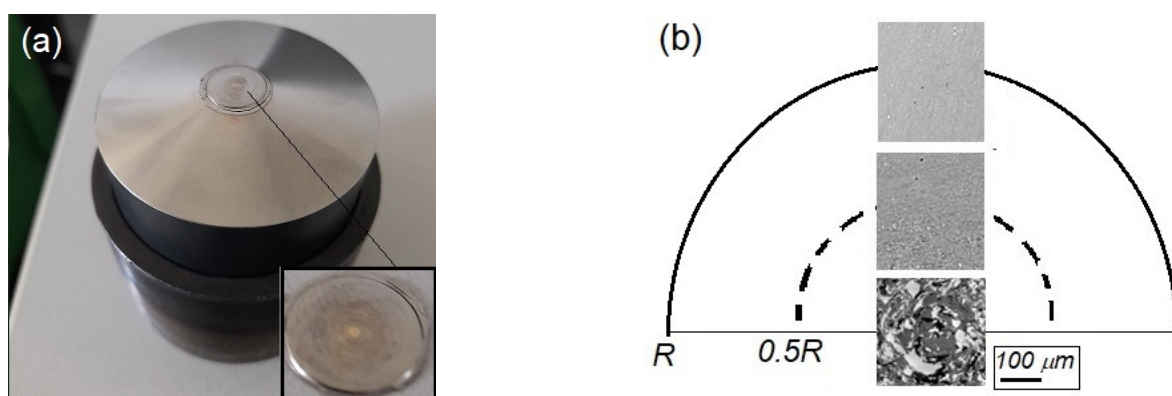

Figure 1. HPT consolidation of a powder mixture. (**a**)—bottom anvil of the HPT rig with the deformed sample; (**b**)—SEM image after ten revolutions, illustrating the change in microstructure from the center to the edge of the sample.

2.2. Vickers Hardness Measurements

To characterize the mechanical properties of RHEAs, Vickers microhardness for all samples after various treatments was determined using Buehler Micromet 5104 (Leinfelden-Echterdingen, Germany). All measurements were carried out at a load of 0.5 N and a

holding time of 10 s. Measurements were conducted in triplicate along three different diameters of round samples; the standard deviation from the average was ~7%.

2.3. Phase Analysis

X-ray diffraction (XRD) analysis of the phases present in the samples was carried out on a PANalytical X'Pert Pro MRD diffractometer (Malvern, UK) with Cu K_{α} radiation (λ = 1.5406 Å) and a 2 × 2 mm aperture size used at 40 kV and 30 mA. Diffraction profiles were recorded in the 2θ range 30–80° with a step size of 0.02° and dwell time of 10 s.

2.4. Microstructure Characterization

The microstructure of samples produced by HPT deformation was characterized using a JEOL 7800 FEG (Tokio, Japan) scanning electron microscope (SEM) at an accelerating voltage of 20 kV and a working distance of 10 mm. Images were acquired using a lower electron detector (LED) equivalent to the SE2 detector.

The microstructure of the samples was also characterized by means of transmission electron microscopy (TEM) on a Themis 300 TEM (Thermo Fischer Scientific, Eindhofen, The Netherlands) equipped with a super-EDS detector. For this purpose, TEM lamellae were prepared using a focused ion beam on an FEI Strata dual-beam facility (Eindhofen, The Netherlands) at 30 kV, followed by final milling at 5 kV.

3. Results and Discussion

As shown in [11], a specific characteristic of HPT that distinguishes it from other SPD processes is the turbulent nature of the plastic flow. This turbulence creates favorable conditions for intensified mass transfer and the intermixing of constituent powders. Moreover, in HPT, it is easy to introduce a level of strain and hydrostatic pressure far exceeding those obtained in other types of SPD. The microstructure and hardness at the center of the sample (0.0 *R*) differ from those at a distance of mid-radius (0.5 *R*) and at the edge of the sample (1.0 *R*) at the beginning of straining. However, after the number of revolutions above five, they gradually saturate to uniform values, as shown in [12]. Our results indicate that even after ten revolutions, differences between the center, mid-radius, and edge are still present. This discrepancy can be explained by the absence of binding between loose powders, which results in a plastic flow significantly different from that of solid materials when subjected to HPT. Nevertheless, this non-uniformity in strain distribution provides us the opportunity to observe phase transformations depending on the distance from the center of the sample and, therefore, on the strain level, which exceeds 40 at the edge of the HPT disk.

3.1. Intermixing Study by STEM-EDX

Insets in Figure 1b already indicate the presence of a vortex of turbulent flow in the central part of a BE powder sample. After ten revolutions, these powders intermix to such an extent that there is no visible difference between the constituents in the outer regions of the HPT disk, particularly at the edge. Previous research [12] has shown that the strain gradient leads rapidly to structural uniformity along the radius, except for a small central region. However, in the case of powders, the attainment of structural uniformity is slower compared to full-dense solid material, and the border between the turbulent flow at the center and that at a distance of 0.5 *R* remains visible after ten revolutions, especially noticeable in the LP-M1-HPT alloy.

The spatial distribution of elements in the samples after plastic deformation was analyzed using STEM-EDX; see the elemental maps in Figures 2 and 3. In both samples, with increasing deformation, an increase in the degree of component mixing is evident. Thus, for the LP-M2-HPT alloy in Figure 3, there is practically no composition variation at the mid-radius and at the edge of the sample. However, for the LP-M1-HPT alloy in Figure 2, noticeable heterogeneity of some elements persists at the same positions on the HPT disk, including the mid-radius.
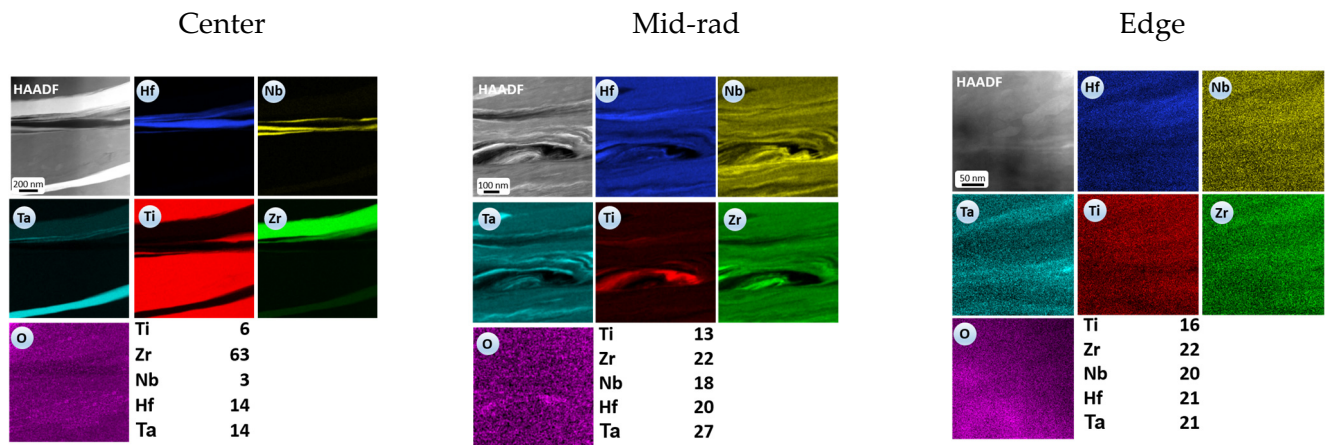
Center

Mid-rad

Edge

Figure 2. STEM-EDX maps (at. %) for M1 alloy show the elemental distribution at various locations of the HPT disk. The table shows the overall composition calculated from EDX spectra for the whole map area.
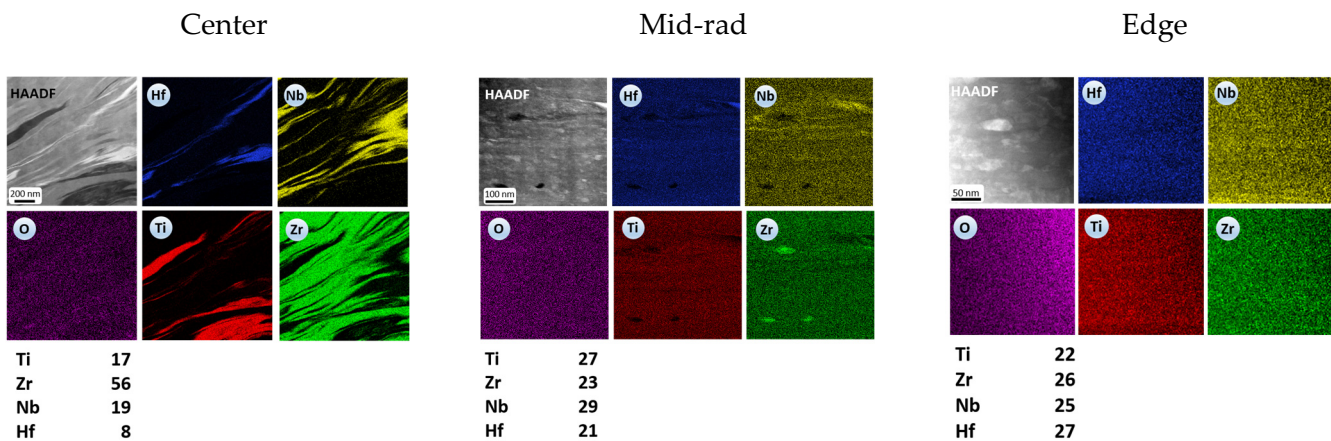
Center

Mid-rad

Edge

Figure 3. STEM-EDX maps (at. %) for M2 alloy show the elemental distribution at various locations of the HPT disk. The table shows the overall composition calculated from EDX spectra for the whole map area.

An important issue is also the presence of oxides in the structure of the material, which could have formed during deformation since the RHEA samples were obtained in the air. To address this issue, in addition to elemental maps of the main elements, oxygen maps are also presented in Figures 2 and 3. It can be seen that oxygen is evenly distributed over the map area, and it belongs to the oxides that inevitably form while transferring samples from the FIB to the TEM. The XRD data presented below also prove that there are no oxide phases in the structure of the samples produced by HPT. It should be noted that direct determination of oxygen content from EDX maps does not give the correct result due to the difficulty of subtracting the background in the region of the O-K line.

3.2. Hardness Characterization

The results of microhardness measurements for alloys after HPT deformation and after short-term annealing at 500 °C are shown in Figure 4. For both alloys, after deformation, a slight increase in the level of hardness is observed in the edge region of the sample compared to the central part, approximately by HV 85 for M1 and by HV 60 for M2. The visible difference between the two samples is the higher hardness value for alloy M1 compared to alloy M2. Annealing of the alloys, even at a relatively low temperature, led to a noticeable increase in hardness at the edge of the sample, while the HV kept close values for the center and mid-radius. The increase in hardness upon annealing was caused

by HV 115 for M1 and HV 160 for M2. The phenomenon of hardness increase due to annealing in SPD materials has been observed by several researchers and discussed in our recent publication [7]. Several factors may contribute to such an increase in hardness after annealing, including phase transformation and agglomeration [7] or the annihilation of deformation-induced vacancies [13]. Additionally, the increase in the volume fraction of hcp phases, as will be discussed in Section 3.3, may also contribute to the increase in hardness.
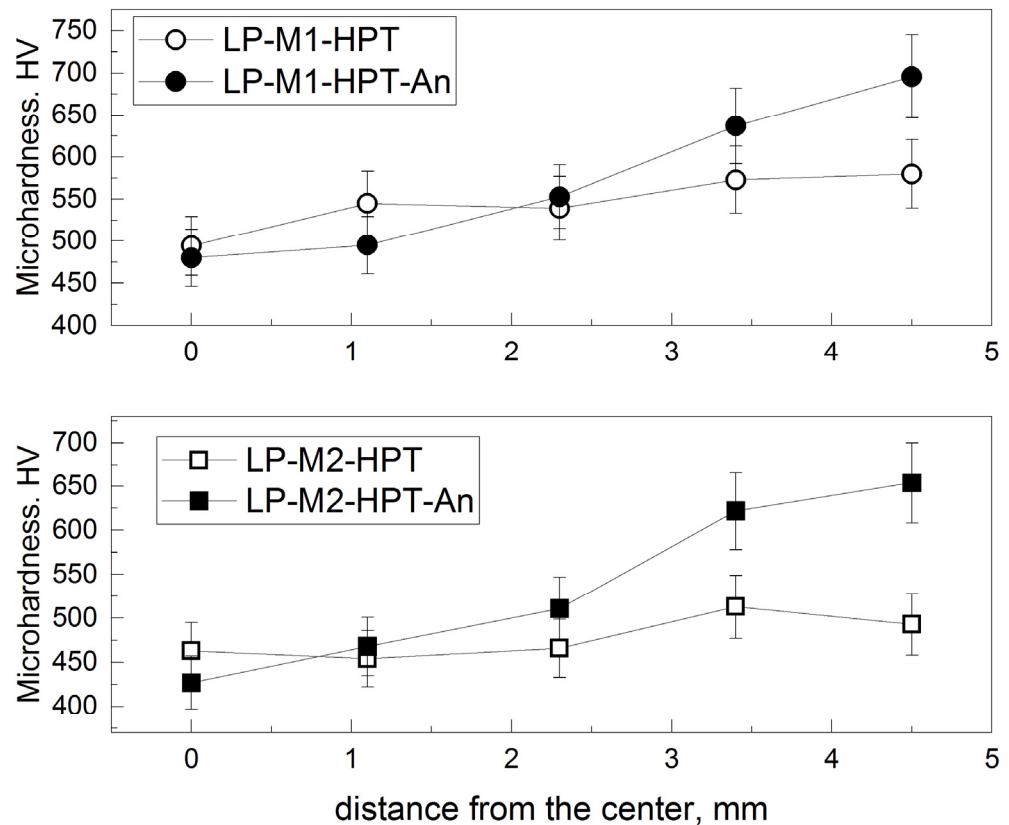

Figure 4. Vickers microhardness was measured along the HPT disc radius after HPT deformation and after short-term annealing at 500 °C for (**top**) M1 and (**bottom**) M2 alloys.

3.3. Definition of Phase Formation by XRD Analysis

The analysis of the three spectra corresponding to positions at the center, mid-radius, and edge of the HPT disk, along with the spectra of the initial powder mixture, provides a comprehensive overview of the formation and evolution in the phase composition due to plastic deformation. It is important to note that in the deformed state, three new phases, in fact corresponding solid solutions, are formed: the bcc phase, the hcp1 phase with parameters close to those of Zr (JCPDS #034-0657), and the hcp2 phase with parameters close to those of α-Ti (JCPDS #044-1294); the corresponding phase designations are used, respectively, in Figure 5 and Table 1.

Both samples display similar diffraction patterns, indicating the same sequence of phase transformations with plastic strain. For the LP-M2-HPT sample, XRD phase analysis reveals several notable changes.

In the central part of the HPT disk, the diffraction patterns clearly show peaks associated with three phases: First, the individual peaks of Zr and Hf (JCPDS #038-1478) of the original sample merge as a result of deformation, and the hcp1 phase is formed in the structure. Secondly, the structure contains a bcc phase with a parameter close to Nb (JCPDS #034-0370). The third phase, hexagonal hcp2, is formed on the basis of the α-Ti lattice. The deviation of their parameters from those of pure components reflects the formation of solid solutions through mutual dissolution. As the strain increases, the peak intensity of the

hcp2 phase gradually decreases to the background level, suggesting that the edge region of the sample consists of only two phases, i.e., bcc and a small amount of hcp1.
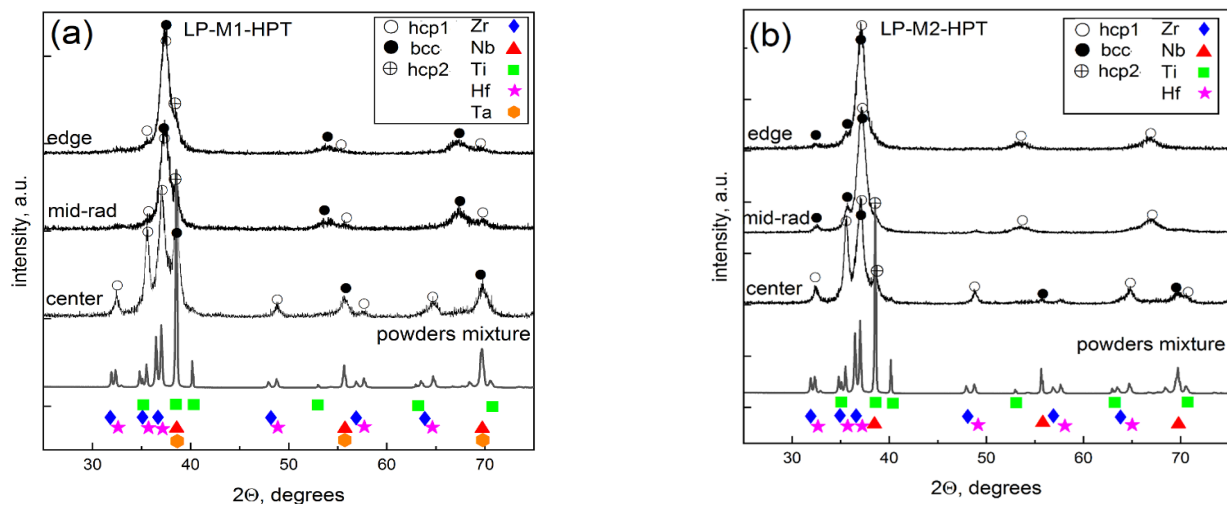

Figure 5. XRD profiles from initial BE mixtures and samples. (**a**)—LP-M1-HPT; and (**b**)—LP-M2-HPT.

Table 1. Phase composition and lattice parameters of the constituent phases of the two studied alloys after HPT deformation.

		Center		Mid-Radius		Edge	
		Fraction, %	Lattice, Å	Fraction, %	Lattice, Å	Fraction, %	Lattice, Å
LP-M1-HPT	hcp1	48	a = 3.202 c = 5.063	2	a = 3.215 c = 5.109	0	a = 3.202 c = 5.063
	bcc	49	a = 3.304	93	a = 3.400	98	a = 3.304
	hcp2	3	a = 2.951 c = 4.662	5	a = 3.051 c = 4.672	2	
LP-M2-HPT	hcp1	54	a = 3.202 c = 5.063	5	a = 3.188 c = 5.063	2	a = 3.202 c = 5.063
	bcc	28	a = 3.304	95	a = 3.404	98	a = 3.304
	hcp2	18	a = 2.951 c = 4.662	0		0	

Examination of the XRD spectra of LP-M1-HPT shows that due to insignificant differences in the lattice parameters of pure Nb and Ta (JCPDS #004-0788), it is almost impossible to distinguish their peaks in the initial powder mixture, and even more so after deformation. In addition to transformations observed in the LP-M2-HPT alloy, the LP-M1-HPT sample shows that under significant deformation (at the mid-radius and edge), two phases are present: bcc with a parameter close to Nb and hexagonal hcp2 based on an α-Ti lattice, suggesting that the addition of refractory Ta stabilizes the hcp2 phase.

The phase parameters and composition determined by the Rietveld refinement method are given in Table 1.

The XRD spectra of the samples after annealing for three positions, at the center, mid-radius, and at the edge, are shown in Figure 6; the phase composition and phase parameters determined by the Rietveld refinement method are given in Table 2. It should be noted that annealing for 1 h at a temperature of 500 °C led to significant changes in the phase composition of the studied samples, as can be seen by changes in the lattice parameters of the phases. Moreover, the α-Ti-based hcp2 phase completely dissolved after annealing, while the Hf-based hcp3 phase appeared in both alloys. For the LP-M1-HPT-An alloy, with increasing distance from the center, the fraction of the hcp1 Zr-based phase continuously

increases, the fraction of the cubic phase simultaneously decreases, and the fraction of hcp3 decreases until complete disappearance at the edge of the sample.
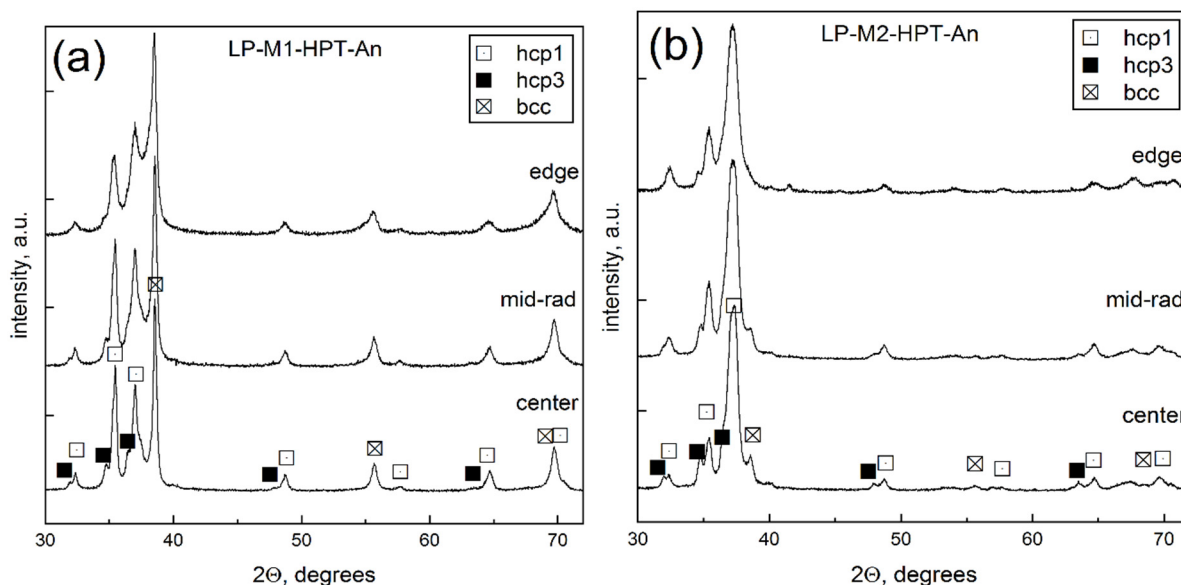

Figure 6. XRD profiles from the annealed samples (**a**)—LP-M1-HPT-An and (**b**)—LP-M2-HPT-An.

Table 2. Phase composition and lattice parameters of the constituent phases of the two studied alloys after HPT deformation followed by annealing.

		Center		Mid-Radius		Edge	
		Fraction, %	Lattice, Å	Fraction, %	Lattice, Å	Fraction, %	Lattice, Å
LP-M1-HPT-An	hcp1	32	a = 3.192	40	a = 3.184	67	a = 3.199
			c = 5.063		c = 5.054		c = 5.161
	bcc	59	a = 3.299	57	a = 3.295	33	a = 3.306
	hcp3	9	a = 3.237	3	a = 3.229	0	
			c = 5.161		c = 5.160		
LP-M2-HPT-An	hcp1	84	a = 3.179	78	a = 3.182	93	a = 3.178
			c = 5.086		c = 5.101		c = 5.074
	bcc	13	a = 3.305	6	a = 3.314	0	
	hcp3	3	a = 3.242	16	a = 3.246	7	a = 3.246
			c = 5.182		c = 5.192		c = 5.193

For the LP-M2-HPT-An alloy, a similar trend can be noted in the change in the hcp1 phase fraction, while the cubic phase disappears, and at the edge of the sample, the structure contains mainly the hcp1 phase with a small fraction of the hexagonal phase hcp3.

3.4. Microstructure Characterization by TEM

The gigantic plastic deformation induced by HPT led to several outcomes: the formation of solid, fully dense material; effective intermixing of BE powders into a uniform mixture; the formation of new phases of RHEAs; and exceptional grain refinement, resulting in grain sizes below 100 nm.

To demonstrate grain refinement, Figure 7 displays bright-field (BF) and dark-field (DF) TEM micrographs of the LP-M1-HPT and LP-M2-HPT alloys acquired at the edge of the HPT disk. Through the analysis of the corresponding images for all three positions on the disk, the average grain size was calculated with the values presented in Table 3. The corresponding selected area electron diffraction patterns are shown as an inset in Figure 7

and provide information on the phase composition of the alloys, which coincides with data obtained from XRD spectra. The formation of nanostructured RHEAs by room-temperature HPT explained the high values of Vickers microhardness presented in Figure 4, especially in the outer region of the discs (mid-radius and edge).
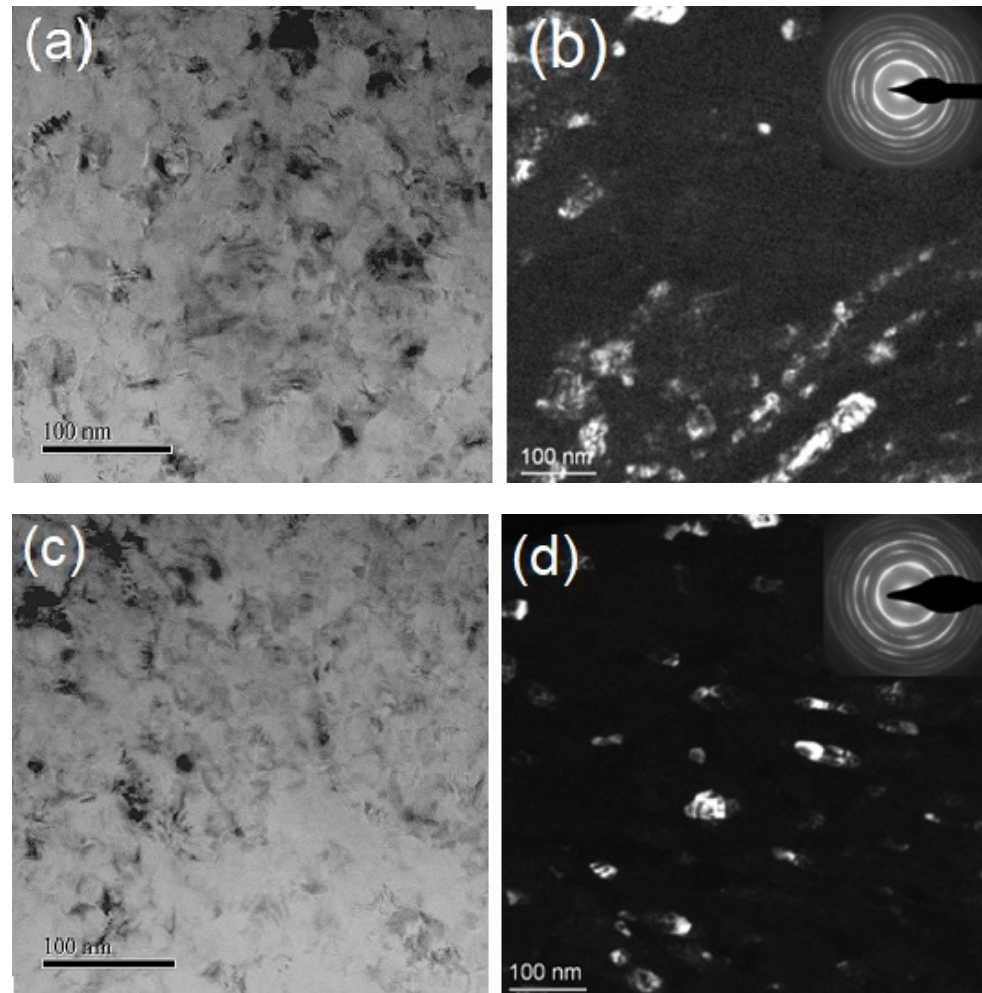

Figure 7. BF and DF TEM images of the alloys and the corresponding electron diffraction patterns (insets). The images were collected at the edge region of the HPT disc. (**a**,**b**)—LP-M1-HPT; (**c**,**d**)—LP-M2-HPT.

Table 3. Average grain size (nm) for two alloys based on the corresponding DF-TEM images from different locations on the HPT disk.

	Center	Mid-Rad	Edge
LP-M1-HPT	82	36	35
LP-M2-HPT	92	39	30

Figure 8 shows STEM-BF images of samples at mid-radius after annealing at 500 °C for one hour. Relaxation of internal stresses due to annealing led to the dislocation's rearrangement by their movement to the grain boundaries and the formation of the clearly defined microstructure shown in Figure 8. It is noteworthy that after annealing, the microstructure of both compositions, M1 and M2, remains ultrafine-grained (average grain size 60 nm and 100 nm for M1 and M2 alloys, respectively), with insignificant grain growth resulting in observed bimodality of microstructure. Although the bimodal nature of the grain size distribution for both alloys is observed after annealing, only a small fraction

(below 0.04) of grains reaches a size of 200 ± 50 nm. This suggests that elements in the solid solution limit grain boundary mobility, minimizing grain growth. Moreover, short, low-temperature annealing resulted in a further increase in Vickers microhardness, which is presumably associated with the transformation of the BCC phase into new phases.
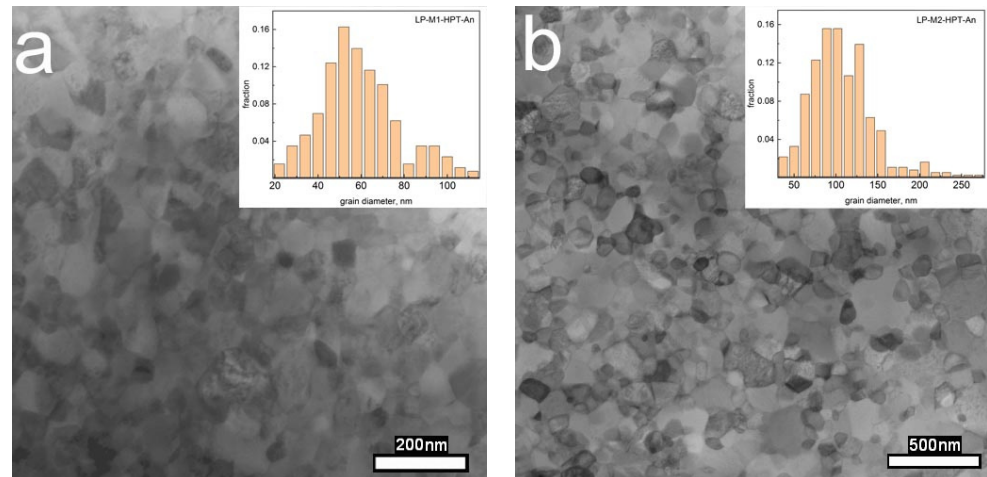

Figure 8. BF-STEM images of the alloys after HPT deformation followed by annealing at 500 °C for 1 h for the mid-radius of the sample. The insets show the grain size distribution for (**a**)—LP-M1-HPT-An and (**b**)—LP-M2-HPT-An.

Comparison to the most currently published works on equiatomic M1 and M2 alloys indicates a tendency towards the formation of a single bcc phase as a result of arc-melting production [1–5]. Furthermore, these alloys maintain their bcc single-phase structures even during subsequent HPT processing [14]. Interestingly, in comparison to these studies, the new production route [7], consisting of preliminary warm compaction by ECAP followed by HPT at room temperature, has shown the presence of two phases after combined deformation, e.g., bcc and hcp. As discussed here, the application of HPT to loose powders results in the appearance of three phases, namely bcc, hcp1, and hcp2. This suggests that the new method of synthesizing RHEAs by room-temperature HPT provides a degree of freedom to obtain multiphase material depending on the strain level.

It has been found previously [14–16] that any heat treatment of nanocrystalline M1 and M2 below 1000 °C results in the decomposition of the bcc phase, typically into the bcc and hcp phases. It should be noted that the decomposition of the bcc phase is typically observed after annealing following plastic deformation. HPT processing is often used to introduce different levels of plastic strain into the material [14]. For example, in [16], annealing at a temperature of 467 °C caused the decomposition of the single-phase bcc M2 alloy into two different bcc structures with lower and higher lattice constants compared to the initial state. Subsequent heat treatments conducted between 467 and 617 °C resulted in the nucleation of a Zr/Hf-rich hcp phase, albeit with a low volume fraction. Similarly, as discussed in [14,16], the major bcc phase exhibited two components with higher and lower lattice parameters and a ZrHf-rich hcp phase for the M2 alloy. On the contrary, for M1 alloys, only two phases, hcp and bcc, were observed after annealing. Comparable results on phase decomposition and thermal stability were predicted by the modeling for M1 and M2 RHEAs published in [17,18]. The emergence of two HCP phases in this study due to severe plastic deformation introduced by HPT suggests a potential for optimizing properties through adjustments of strain levels and annealing parameters.

Therefore, an analysis of all publications on these two compositional systems of RHEAs, including recent ones [19–24], shows that neither experimental data [19–22] nor theoretical predictions [17,18,24] and machine learning [23] have been instrumental in discovering a new method for producing multi-phased RHEAs through severe plastic deformation at room temperature.

4. Conclusions

For the first time, the refractory high-entropy alloys with equiatomic compositions, HfNbTaTiZr and HfNbTiZr, were synthesized directly from a blend of elemental powders at room temperature using high-pressure torsion.

HPT was shown to create a homogeneous atomic mixture in the outer region of the disks, where the strain level reached 40 and an ultrafine-grained microstructure with grain sizes ranging from 30 to 40 nm was formed.

In contrast to RHEAs produced by molten routes, both alloys in the outer region of the disc underwent the formation of three new phases: Zr-based hcp1 phase, α-Ti-based hcp2 phase, and Nb-based bcc phase. The volume fraction of the hcp2 phase gradually decreased with increasing strain in both alloys, resulting in two-phase alloys at the edges of the samples in the LP-M2-HPT alloy. A similar tendency was observed for the LP-M1-HPT alloy, although a small fraction of the hcp2 phase was identified as a result of the stabilizing effect of Ta.

A short low-temperature annealing revealed a significant relaxation of the microstructure with a slightly increased grain size, although still below 100 nm. Meanwhile, the phase composition of the samples after annealing changed significantly. For the M1 alloy, annealing leads to the formation of a mixed structure consisting of the new two hexagonal and cubic phases in different proportions depending on the distance to the center of the HPT disk and, therefore, on the level of accumulated plastic strain. Alloy M2 consists predominantly of a hexagonal phase with a small admixture of a component with a cubic structure. An increase in Vickers hardness in the outer regions of the samples is attributed to the transformation of the BCC phase into new phases.

References

1. Miracle, D.B.; Senkov, O.N. A critical review of high entropy alloys and related concepts. *Acta Mater.* **2017**, *122*, 448–511. [CrossRef]
2. Koch, C.C. Nanocrystalline high-entropy alloys. *J. Mater. Res.* **2017**, *32*, 3435–3444. [CrossRef]
3. Ren, X.; Li, Y.; Qi, Y.; Wang, B. Review on preparation technology and properties of refractory high entropy alloys. *Materials* **2022**, *15*, 2931. [CrossRef]
4. Senkov, O.N.; Miracle, D.B.; Chaput, K.J.; Couzinie, J.-P. Development and exploration of refractory high entropy alloys-A review. *J. Mater. Res.* **2018**, *33*, 3092–3128. [CrossRef]
5. Senkov, O.N.; Miller, J.D.; Miracle, D.B.; Woodward, C. Accelerated exploration of multi-principal element alloys with solid state solution phases. *Nat. Commun.* **2015**, *6*, 6529. [CrossRef]
6. Lapovok, R.; Tomus, D.; Muddle, B. Low-temperature compaction of Ti–6Al–4V powder using equal channel angular extrusion with back pressure. *Mater. Sci. Eng. A* **2008**, *490*, 171–180. [CrossRef]

7. Lapovok, R.; Ferdowsi, M.R.G.; Shterner, V.; Hodgson, P.D.; Mazilkin, A.; Boltynjuk, E.; Kulagin, R.; Semiatin, S.L. Refractory High-Entropy Alloys Produced from Elemental Powders by Severe Plastic Deformation. *Adv. Eng. Mater.* **2024**, *26*, 2301949. [CrossRef]

8. Málek, J.; Zýka, J.; Lukáč, F.; Vilémová, M.; Vlasák, T.; Čížek, J.; Melikhova, O.; Macháčková, A.; Kim, H.-S. The effect of processing route on properties of HfNbTaTiZr high entropy alloy. *Materials* **2019**, *12*, 4022. [CrossRef] [PubMed]

9. Málek, J.; Zýka, J.; Lukáč, F.; Čížek, J.; Kunčická, L.; Kocich, R. Microstructure and mechanical properties of sintered and heat-treated HfNbTaTiZr high entropy alloy. *Metals* **2019**, *9*, 1324. [CrossRef]

10. Lukáč, F.; Vilémová, M.; Klementová, M.; Minárik, P.; Chráska, T. The origin and the effect of the fcc phase in sintered HfNbTaTiZr. *Mater. Lett.* **2021**, *286*, 129224. [CrossRef]

11. Kulagin, R.; Beygelzimer, Y.; Ivanisenko, Y.; Mazilkin, A.; Hahn, H. High Pressure Torsion: From Laminar Flow to Turbulence. *IOP Conf. Ser. Mater. Sci. Eng.* **2017**, *194*, 012045. [CrossRef]

12. Straumal, B.B.; Kulagin, R.; Klinger, L.; Rabkin, E.; Straumal, P.B.; Kogtenkova, O.A.; Baretzky, B. Structure Refinement and Fragmentation of Precipitates under Severe Plastic Deformation: A Review. *Materials* **2022**, *15*, 601. [CrossRef] [PubMed]

13. Cízek, J.; Hausild, P.; Cieslar, M.; Melikhova, O.; Vlasak, T.; Janecek, M.; Kral, R.; Harcuba, P.; Lukac, F.; Zýka, J.; et al. Strength enhancement of high entropy alloy HfNbTaTiZr by severe plastic deformation. *J. Alloys Compd.* **2018**, *768*, 924–937. [CrossRef]

14. Hung, P.T.; Kawasaki, M.; Han, J.-K.; Lábár, J.L.; Gubicza, J. Thermal stability of a nanocrystalline HfNbTiZr multi-principal element alloy processed by high-pressure torsion. *Mater. Charact.* **2020**, *168*, 110550. [CrossRef]

15. Schuh, B.; Volker, B.; Todt, J.; Schell, N.; Perriere, L.; Li, J.; Couzinie, J.P.; Hohenwarter, A. Thermodynamic instability of a nanocrystalline, single-phase TiZrNbHfTa alloy and its impact on the mechanical properties. *Acta Mater.* **2018**, *142*, 201–212. [CrossRef]

16. Cao, P.; Huang, H.; Jiang, S.; Liu, X.; Wang, H.; Wu, Y.; Lu, Z. Microstructural stability and aging behavior of refractory high entropy alloys at intermediate temperatures. *J. Mater. Sci. Technol.* **2022**, *122*, 243–254. [CrossRef]

17. Chen, S.-M.; Ma, Z.-J.; Qiu, S.; Zhang, L.-J.; Zhang, S.-Z.; Yang, R.; Hu, Q.-M. Phase decomposition and strengthening in HfNbTaTiZr high entropy alloy from first-principles calculations. *Acta Mater.* **2021**, *225*, 117582. [CrossRef]

18. Li, T.; Wang, S.; Fan, W.; Lu, Y.; Wang, T.; Li, T.; Laaw, P.K. CALPHAD-aided design for superior thermal stability and mechanical behavior in a TiZrHfNb refractory high-entropy alloy. *Acta Mater.* **2023**, *246*, 118728. [CrossRef]

19. Yang, W.; Pang, S.; Liu, Y.; Wang, Q.; Liaw, P.K.; Zhang, T. Design and properties of novel Ti-Zr-Hf-Nb-Ta high-entropy alloys for biomedical applications. *Intermetallics* **2022**, *141*, 107421. [CrossRef]

20. Huang, Y.-C.; Lai, Y.-C.; Lin, Y.-H.; Wu, S.-K. A study on the severely cold-rolled and annealed quaternary equiatomic derivatives from quinary HfNbTaTiZr refractory high entropy alloy. *J. Alloys Compd.* **2020**, *855*, 157404. [CrossRef]

21. Huang, H.; Sun, Y.; Cao, P.; Wu, Y.; Liu, X.; Jiang, S.; Wang, H.; Lu, Z. On cooling rates dependence of microstructure and mechanical properties of refractory high-entropy alloys HfTaTiZr and HfNbTiZr. *Scr. Mater.* **2022**, *211*, 114506. [CrossRef]

22. He, Q.; Yoshida, S.; Tsuji, N. Characteristic strengthening mechanisms in body-centered cubic refractory high/medium entropy alloys. *Scr. Mater.* **2023**, *231*, 115442. [CrossRef]

23. Sun, Y.; Lu, Z.; Liu, X.; Du, Q.; Xie, H.; Lv, J.; Song, R.; Wu, Y.; Wang, H.; Jiang, S.; et al. Prediction of Ti-Zr-Nb-Ta high-entropy alloys with desirable hardness by combining machine learning and experimental data. *Appl. Phys. Lett.* **2021**, *119*, 201905. [CrossRef]

24. Nataraj, C.M.; van de Walle, A.; Samanta, A. Temperature-Dependent Configurational Entropy Calculations for Refractory High Entropy Alloys. *J. Phase Equilib. Diffus.* **2021**, *42*, 571–577. [CrossRef]